Evaluation of Electrospun Fibrous Mats Targeted for Use as Flow Battery Electrodes

Selina Liu,[a] Matt Kok,[a,*] Yongwook Kim,[b] John L. Barton,[c,d,*] Fikile R. Brushett,[c,d,] and Jeff Gostick[a,b,**,z]**

[a]*McGill University, Montreal, QC H3A2B2, Canada*
[b]*University of Waterloo, Waterloo, Ontario N2L3G1, Canada*
[c]*Massachusetts Institute of Technology, Cambridge, Massachusetts 02139, USA*
[d]*Joint Center for Energy Storage Research, USA*

Electrospinning was used to create custom-made fibrous electrode materials for redox flow batteries with targeted structural properties. The aim was to increase the available surface area for electrochemical reaction without diminishing the transport properties of the electrode. Electrospinning conditions were identified that could produce fibers several times larger than those typically yielded by the technique, yet much smaller than in commercially available electrodes. These materials were subsequently carbonized using widely reported protocols. The resultant materials were subjected to a range of characterization tests to confirm that the feasibility of the target material, including surface area, pore and fiber sizes, porosity, conductivity, and permeability. The most promising material to emerge from this selection processes was then tested for electrochemical performance in a flow cell. The produced material performed markedly better than a commercially available material. Further optimizations such as improved consistency in the production and some surface activation treatments could provide significant advancements.

Manuscript submitted April 20, 2017; revised manuscript received June 21, 2017. Published July 14, 2017. This was Paper 23 presented at the Honolulu, Hawaii, Meeting of the Society, October 2–7, 2016.

With the broadening adoption of intermittent renewable energy, large scale energy storage is becoming essential.[1] Redox flow batteries are a promising option due to their decoupled energy and power capacity, geographic flexibility, breadth of chemistry options, and ease of scale-up.[1,2] Despite the first prototypes being proposed by NASA in the 1970's,[3] the technology has yet to reach mass commercialization due to cost ($/kWh and $/kW). Key parameters that define flow battery cost include volumetric energy density, materials, cell voltage, area-specific resistance (ASR),[4,5] lifetime, and membrane selectivity. Liquid electrolytes are stored in tanks, and pumped to electrochemical cells where the redox reactions occur at the solid-liquid interface of porous electrodes during charging or discharging. To achieve higher reaction rates, and therefore higher efficiency, the electrodes should have good catalytic activity for the reaction. However, since the materials choices are limited by durability, chemical compatibility and cost, the use of simple carbon or graphite electrodes is common. If the kinetics cannot be improved in a cost-effective manner, then an alternative route to improving reaction rates is to increase active surface area. Currently, the most commonly-used material for flow battery electrodes is commercially available carbon-fiber paper developed for use as the gas diffusion layer (GDL) of PEM fuel cells. Attempts to increase performance of these carbon papers include stacking multiple layers,[6–8] laser etching holes,[9] growing carbon nanotubes on fiber surfaces[10,11] and thermal activation.[12]

These efforts to improve cell performance of flow batteries are driven by increasing the current density of the cell (A/m^2). In the case of stacking multiple layers and growing nanotubes of the fiber surfaces, this creates more surface area per unit area of cell. These two methods are not entirely equal however, as the former does not increase the volumetric current density (A/m^3) since N layers increases the fiber surface area N times, but also the volume by the same factor N. Using thicker electrodes has limitations since it increases the transport lengths for the ionic species to reach the reactive sites. The case of growing nanotubes on the fiber surface does increase the volumetric current density, but the process is costly and complex. It is also not certain that all of the added surface area will be used since mass transfer limitations may occur within the grown nanofiber array. An alternative approach to increasing the volumetric current density is to make a fibrous electrode with fibers that are smaller than the currently used materials.

As a first approximation, the specific surface area, A_s, (m^2/m^3) of a fibrous material can be estimated by assuming that all of the solid in the bulk volume is a continuous filament of diameter d_f. The length, L, of this filament is based on the solid volume which can be determined from the mass of the electrospun mat, m, and the skeletal density of the solid, ρ_s, and the cross-sectional area of the fibers, A_C:

$$L = \frac{V_s}{A_C} = \frac{m/\rho_s}{\frac{\pi}{4}d_f^2} \quad [1]$$

The specific surface area of this single fictitious filament is then found from:

$$A_s = \frac{\pi d_f L}{V_b} \quad [2]$$

where V_b is the bulk volume of the mat. Eq. 2 can be simplified by inserting Eq. 1 for L and noting that the solid volume V_S can be expressed as $V_b(1-\epsilon)$:

$$A_s = \frac{4(1-\varepsilon)}{d_f} \quad [3]$$

where $\epsilon = \frac{V_{pore}}{V_{bulk}}$ is the porosity of the mat. This is sometimes referred to as the filament analogue (FA) model,[13] and it provides a useful estimate about the interplay between fiber size and the porosity of the mat. Specifically, smaller fibers and lower porosity lead to more specific surface area since these both result in more fibers per unit volume.

Improving cell performance is not as straightforward as using a tightly packed array of smaller fibers however. The permeability coefficient, K, of the mat must also be considered since it controls how easily liquid reactant flows through the electrode, as governed by Darcy's law:

$$Q = \frac{KA}{\mu L}\Delta P \quad [4]$$

where Q is the volumetric flow rate of the fluid (m^3/s), A is the cross sectional area of the fluid flow (m^2), μ is the viscosity of the fluid

*Electrochemical Society Student Member.
**Electrochemical Society Member.
[z]E-mail: jgostick@uwaterloo.ca

Table I. Summary of material properties.

	PAN wt%	Porosity	Fiber Diameter [um]	Electrical Conductivity [S/m]	Thickness [um]	Specific Surface Area [m^2/g]
Electrospun	10	94.67 ± 0.54	0.70 ± 0.30	—	758 ± 233	—
	11	94.74 ± 0.66	0.94 ± 0.13	—	741 ± 282	—
	12	93.47 ± 1.28	1.14 ± 0.19	—	770 ± 374	—
	13	91.99 ± 1.38	1.39 ± 0.30	—	604 ± 315	—
Carbonized	10	88.65 ± 2.14	0.50 ± 0.17	1519	227 ± 41	—
	11	90.42 ± 1.72	0.56 ± 0.10	—	249 ± 93	—
	12	89.10 ± 2.13	0.76 ± 0.18	1280 ± 176	281 ± 121	2.94
	13	85.30	1.22 ± 0.64	—	255 ± 52	—

(Pa·s), ΔP is the pressure drop (Pa) across length L (m). Darcy's law shows that for a given pressure, a higher K will result in higher reactant flow rates, and higher interstitial velocity which implies improved mass transfer. For a fibrous material, its permeability coefficient is well correlated by the Carmen-Kozeny equation:[14–16]

$$K = \frac{d_f^2 \varepsilon^3}{16 k_{ck} (1-\varepsilon)^2} \quad [5]$$

The value k_{ck} is a fitting parameter, which accounts for the material structure that is not indicated in the porosity and fiber diameter, such as fiber morphology and shape. For example, granular porous materials have different k_{ck} from fibrous material,[17] and aligned fibrous material have different k_{ck} value from randomly aligned fibers.[18] Eq. 5 shows that the permeability coefficient decreases sharply with decreasing fiber size and porosity, and suggests that efforts to increase surface area according to Eq. 3 will be at the expense of flow properties of the electrode.

The competition between specific surface area and permeability creates an optimization problem to find the values of porosity and fiber diameter that will result in the best overall cell performance. Recently, Kok et al.[19] used multi-physics modeling to study the effect of various physical properties of fibrous electrodes on transport properties and performance of a flow battery, with the aim of predicting optimal electrode properties. The results showed that a fiber diameter around 1 to 2 μm coupled with a high porosity above 85% yielded the best performance in terms of peak power density. This is much different than the commercially available materials which have fiber diameter around 10 μm and porosity around 80%.

With this information at hand, it was of interest to produce actual materials with these optimized parameters for practical testing. Electrospinning is a useful technique for producing prototype fibrous materials with the desired characteristics. Electrospinning can utilize a wide variety of polymeric materials and easily control the fibrous morphology, therefore creating a wide range of advanced materials for applications such as filtration, sensing, and tissue engineering.[20] However, for use in flow cells, the electrode needs to conduct electrons, provide catalytic activity, and be chemically compatible with the harsh acidic environment. This practically limits the choice to a polymer that can be carbonized. Polyacrylonitrile (PAN) was chosen since it is an excellent carbon fiber precursor[21] due to its high theoretical carbon yield. In addition, electrospinning PAN has been well researched and optimized.[22,23] The literature in this field is focused on the use of PAN as a carbon fiber precursor.[21,24] Although the chemical and physical property transition during carbonization is well-known,[25] the effect of carbonization on transport properties of electrospun materials remains undetermined. In addition, the production of carbon fiber via electrospinning favors small fibers, with reported fiber diameters typically less than 300 nm,[26,27] which is well below the range of optimized fiber diameter.[19] Several review papers[28–31] have specifically summarized the applications of electrospun carbon fiber mats in various energy storage applications, including super capacitors, fuel cells, and Li-ion batteries, but less attention has been directed toward flow batteries. Two groups have explored and tested electrospun electrodes in a flow battery,[32,33] but they focused on the impact of carbonization and surface chemistry on the reaction kinetics of vanadium for all-vanadium cells. To date, no study has been done to optimize cell performance by modifying the material structure to enhance transport properties. These properties must be characterized to understand their effect on the performance of the flow battery. This study offers an extensive characterization of electrospun mats before and after carbonization, by looking at all the key transport properties including material thickness, fiber diameter, porosity, electrical conductivity, and permeability. The performance of these custom-made materials is then evaluated in a flow battery test and compared to off-the-shelf materials.

Experimental Techniques

The electrospun mats were made using a custom-built setup, and then carbonized in an inert-environment furnace to produce a carbonaceous electrode. Various properties were measured before and after carbonization. This section will first describe the material production process, followed by descriptions of the numerous characterization methods applied, ending with the protocols used for in-situ performance testing. A summary of all materials produced is given in Table I.

Material production.—*Electrospinning.*—Electrospinning was performed with custom-built device consisting of a rotating drum of 4 in. (10 cm) diameter, a syringe pump, a linear motion actuator, and a high-voltage power supply. The linear motion actuator was used to raster the needle back and forth across the drum to increase the coating width and ensure an even deposition of fibers on the drum. A negative-polarity power supply (Glassman, MJ30N0400-11) was used with the negative terminal connected to the collector. All other instruments were grounded to ensure safety. The polarity of the power supply was very important to the fiber sizes and stability of electrospinning. In a previous study, Ali et al.[34] found that fiber diameter was larger when the collector is charged rather than the needle, which is the more typical electrospinning configuration. By charging the collector with a negative voltage, the electrospinning process also remained stable for a longer period of time, which was essential in producing samples with the required thickness.

Polyacrylonitrile (PAN) (Sigma, MW 150,000) was the chosen polymer due to its high carbon yield. The spinning solution was prepared by dissolving PAN in N,N-dimethylformamide (DMF) (Sigma, anhydrous, 99.8%) to a varying composition between 10 and 13 wt%. This range of concentrations was selected because higher solution concentrations are known to increase the fiber diameter.[35] The solution was stirred for 20 h without heating to ensure homogeneity without thermal degradation. All samples were electrospun with a 16-gauge (1.194 mm inner diameter) needle, 15 kV applied voltage, a needle to collector distance of 15 cm, collector rotation speed of 5 m/min (measured with a tachometer), and raster length of 6 in. (15 cm), and raster speed of 5 mm/s. Flow rate was slowly decreased throughout spinning to maintain steady spinning conditions, from 0.8 mL/h to 0.5 mL/h. Each electrospun mat was made by spinning 30 mL of solution.

Carbonization.—Following electrospinning, the material was cut into pieces 5 cm by 20 cm and carbonized in a tube furnace, between two alumina plates approximately 1/8" (0.3175 cm) thick. These plates were essential for ensuring a flat and compact electrode. The spacing between the plates was controlled using stainless steel spacer shims that were slightly thinner than the mat to prevent excessive compression. Although it was not explored in the present work, altering the spacing could provide a convenient means of changing the final porosity of the material since they are carbonized in a compressed form. The carbonizing of PAN fibers is a well-documented procedure, and typical conditions were used here.[24,26,36] The material was first stabilized in air, with a heating rate of 5°C/min and a plateau at 250°C for 75 min. Argon was introduced at 25 sccm after the sample has been stabilized for an hour. The temperature was continually increased at a rate of 5°C/min, plateauing at 850°C and 1050°C both for 40 min.

Material characterization.—*Fiber diameter determination.*—Fiber diameter, d_f, was obtained from scanning electron micrograph (SEM) (HITACHI 35000) images. These images were analyzed in ImageJ to estimate fiber diameter. Line segments were drawn across fibers and the length was taken as the width of fibers. SEM images were obtained from 5 different locations on each mat to ensure a representative range of values, and 30 measurements were taken from each image to estimate the average fiber diameter and the standard deviation. This technique is naturally limited to measuring the fiber diameter on the surface, which may differ from the internal fibers. The nature of electrospinning is that the mats are created in an additive manner, so the surfaces represent a snapshot of the entire electrospinning process which could have varied substantially from top to bottom. A preferred approach would be to use X-ray tomography to visualize the interior of the mat.[37]

Porosity measurement.—Porosity, ε, of the electrospun PAN mat was calculated by measuring the mass and volume of a sample cut by a hole punch with 3/8 in. diameter. Assuming that the electrospun fibers have the same density as PAN (1.184 g/cm^3), the mass of the sample was measured with an analytical balance with 0.0001 g resolution. The ratio of the mass to the PAN density gives the solid volume of the sample. Thickness is a delicate property to measure for highly porous and compressible electrospun mats. Thickness was measured with a force sensitive micrometer, as described by Kok et al.[18] The sample was compressed until a 20 mN force had been applied, which was taken to be the top surface boundary of the electrospun mat. With the known diameter and thickness, the total volume can be calculated. Taking the difference between the total and solid volumes gives the pore volume, which yields the porosity of the electrospun mat.

The porosity of the carbonized electrode could not be obtained with the above method since the density of the carbonaceous material was not known. It was instead obtained using a buoyancy method shown to work well for measuring the porosity of thin fibrous media.[38] Thickness of the carbonized electrode, which was notably stiffer than the PAN mat, was measured with a micrometer equipped with a thumb clutch, with 1 μm resolution and ±0.1 μm accuracy. The sample was then weighed both dry and submerged in a wetting fluid such as silicone oil. Applying Archimedes principle allowed the determination of the solid or skeletal density, which can be used directly to find the solid volume fraction and porosity.

Pore size distribution.—The pore size distribution of the mats was measured using a custom-built porosimeter. The experimental system was a modified version of the setup developed previously for measuring air-water capillary pressure of GDLs.[39,40] A detailed schematic of the specially designed sample holder can be found in the previous works. In the current setup, instead of forcing water in and out of the sample, the sample was initially saturated with a highly wetting fluid under vacuum, then air was injected into the sample to displace the wetting fluid. This approach yielded a capillary pressure curve that is analogous to the more typically used mercury intrusion porosimetry,[41] but with far lower applied pressures due to the lower surface tension of the gas-liquid system. The fluid used was a 5 cSt silicone oil (Clearco) with a surface tension of 19.7 mN/m, compared to 485 mN/m for mercury. The saturated sample was then placed in the sample holder and the wetting fluid is displaced from the sample by applying gas pressure above the sample. The mass of the displaced fluid is measured, which corresponds to the volume of the pores. Capillary pressure, P_c, is the difference between the pressure of the applied gas and the pressure of the liquid, which is kept constant at ambient pressure. The applied gas pressure was increased in stages. The pressure at each stage was held constant until the mass of fluid drained from the sample was stable, which was then recorded.

Capillary pressure curves were produced, from which pore size distributions can be roughly approximated using the Washburn equation:

$$P_c = 2\gamma \frac{\cos(\theta)}{r} \quad [6]$$

where P_c is the capillary pressure, γ is the surface tension of wetting fluid, θ is the contact angle and r is the radius of the pore throat accessible at P_c.

Surface Area.—Specific surface area was measured using gas sorption analysis (Micromeritics TriStar 3000) using nitrogen gas at 77 K. Only carbonized samples were tested for surface area since the degassing procedure involved heating to 120°C, which would have damaged the PAN samples. The samples were cut into small square pieces, 0.5 cm wide to fit into the testing tubes, and a total sample mass of about 0.05 g was tested to ensure a detectable amount of surface area. Surface area was extracted from the isotherms using the standard Brunauer–Emmett–Teller (BET) theory.

Permeability.—In-plane permeability, K, of the electrospun and carbonized materials was measured using a device and techniques developed previously[16] and adapted for electrospun material.[18] Compressed air was supplied at the inlet by a mass flow controller (MKS 1160b series) with a range of 200 sccm. Since the flowing fluid was compressible (i.e. air), the following version of Darcy's Law was used:

$$\frac{P_{in}^2 - P_{out}^2}{2LRT/MW_{air}} = \frac{\mu}{K} m' \quad [7]$$

where P_{in} is the inlet pressure, P_{out} is the outlet pressure, L the length of the sample, R the universal gas constant, T the temperature, MW_{air} the molecular weight of air and m' the mass flux through the sample. The flow rate did not exceed 100 sccm which was sufficiently low that no Forchheimer effect was observed.[16] The inlet pressure was measured by a pressure sensor (Omega PX409, 0–30 psia range), and the outlet pressure was open to atmosphere which was taken from the inlet pressure sensor prior to flowing air and confirmed by comparing to a barometer. A sample of 0.5″ × 2″ was cut and placed in the sample holder. Permeability was measured at varying degrees of compression which was controlled by placing shims of known thickness between the plates prior to tightening them together. The thickness of the shims was known to 1 um.

Electrical conductivity.—In-plane conductivity was measured using the Van der Pauw method[42] using the custom-made sample holder shown in Figure 1. A sample with diameter of 0.5″ was placed on top of the base, with its periphery touching the copper rods that acted as the four conductive contact points. The copper rods were connected to 4 set-screws which allowed easy connections to the electrical testing equipment. A power supply was used to supply a current at one edge, for example between point 1 and 2, and a voltmeter was connected at 3 and 4 to measure the voltage drop. Resistivity was calculated with the following relationship:

$$R_{12,34} = \frac{V_{34}}{I_{12}} \quad [8]$$

where $R_{12,34}$ is the resistivity, V_{34} the voltage drop measured at points 3 and 4, I_{12} the applied current at points 1 and 2. The measurement

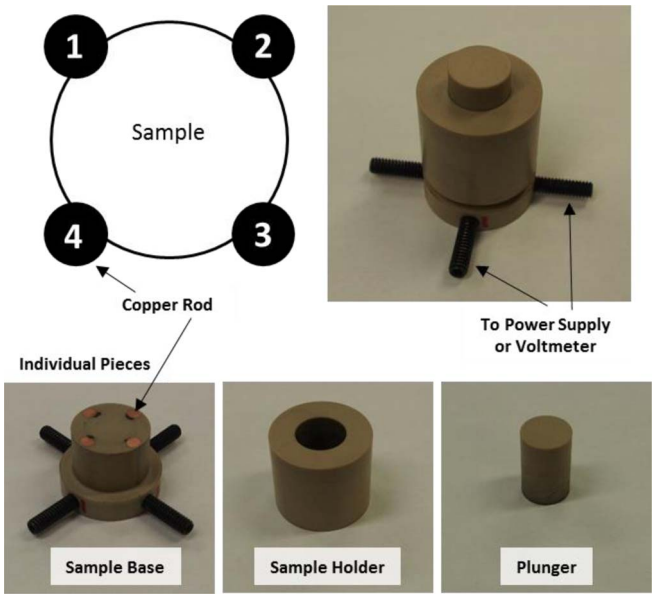

Figure 1. Conductivity sample diagram.

was repeated for the other direction. The sheet resistance, R_s, can then be calculated by finding the value of R_s that satisfies this following equation:

$$e^{-\frac{\pi R_{12,34}}{R_s}} + e^{-\frac{\pi R_{23,41}}{R_s}} = 1 \quad [9]$$

where $R_{12,34}$ and $R_{34,12}$ are resistivity measured with two different configurations. The bulk conductivity, σ_{bulk}, can then be found using:

$$\sigma_{bulk} = \frac{1}{R_s t} \quad [10]$$

where t is the average thickness of the sample.

Flow battery validation.—Characterizing the materials was important to understand the structural and transport properties of the produced materials, but testing in a flow battery was also performed to evaluate the material's viability. The custom-made electrospun electrodes were compared to off-the-shelf material, Sigracet SGL 25AA, as a performance baseline.

Electrolytes.—Vanadyl sulfate hydrate (Alfa Aesar, 99.9% metals basis) and sulfuric acid (Sigma Aldrich, 95.0–98.0%) were purchased and used without further purification. The water content of the vanadyl sulfate hydrate was determined via thermogravimetric analysis (TA instruments SDT Q600). Specifically, approximately 15 mg of powder was added to an alumina pan and set to heat at 10°C/min. to 105°C under nitrogen gas and then held under isothermal conditions for 2 h. The mass lost by the sample, typically ca. 5 wt%, was taken to be the water content and was accounted for in subsequent solution preparation. Stock solutions of electrolytes were prepared using volumetric flasks at room temperature.

Flow cell assembly.—This study used a 2.55 cm^2 flow cell which has been previously reported.[43–45] Backing plates were machined from propylene. Inter-digitated flow fields were machined from 3.18 mm thick impregnated graphite (G347B graphite, MWI, Inc.) with 7 channels (1 mm wide × 0.5 mm deep), 4 inlets and 3 outlets. Either a carbonized electrospun electrode (EE) or pristine Sigracet SGL 25AA electrodes were used in the flow cell. To facilitate comparisons, 2 layers of 25AA were used to maintain a comparable electrode thickness (ca. 400 μm) to the electrospun mat. Each electrode was cut to 1.4 cm × 1.6 cm to allow for sealing within the open gasket area (1.5 cm × 1.7 cm). The PTFE gaskets were selected to be 75–80% of the uncompressed electrode thickness such that when assembled operation, electrode compression was 20–25%. Nafion NR-212 (Nafion Store, Ion Power) was used as a membrane and was soaked in 2.6 M H_2SO_4 overnight prior to use. Electrolyte reservoirs were glass scintillation vials with a rubber septa lid. The septa allowed for inlet and outlet electrolyte tubes as well as a 1/16″ PTFE tube for continuous nitrogen flow and a 21 ga. needle for nitrogen venting. Nitrogen flow was necessary to prevent capacity fade in the presence of oxygen. A peristaltic pump (MasterFlex) with an Easy-Load II pump drive (Cole-Parmer) was used to control electrolyte flowrate through the system. Masterflex Norprene tubing L/S 14 (ID 1.6 mm, OD 4.8 mm, Cole-Parmer) was used to connect the reservoirs, pump head, and flow cell via barbed fittings.

Flow cell testing.—Electrochemical experiments were performed at room temperature using an Arbin Battery Tester (FBTS, Arbin Instruments) for electrolytic preparation, cell cycling, and polarization analyzes and a Bio-Logic VMP-3 for electrochemical impedance spectroscopy (EIS). For all experiments, electrolyte flowrate was fixed at 10 mL/min which was equivalent to a superficial velocity of 0.065 cm/s.[9] This flow rate ensured that at the highest current drawn in these experiments that about 1% of the active species was consumed in the electrode. Nitrogen gas (Airgas, 99.999%) was continuously bubbled through both reservoirs to remove oxygen. The V^{2+}/V^{3+} electrolyte was prepared via electrolysis in a flow cell assembly as reported in previous literature.[6] Specifically, the cell was initially set up with 20 mL of a 50/50 mixture of 1.5 M $VOSO_4$ and 2.6 M H_2SO_4 on the positive side and 10 mL of the same electrolyte mixture on the negative side. The cell was charged via a potentiostatic hold at a cell voltage of 1.7 V until the current density decayed to less than 4 mA/cm^2. This step reduced the V^{4+} to V^{2+} on the negative side and oxidized the V^{4+} to V^{5+} on the positive side. After the charge process, 10 mL of the V^{4+}/V^{5+} electrolyte was removed from its reservoir to balance the electrolyte capacity. After the initial electrolyte charging, the cell was then discharged at 100 mA/cm^2 to 0.6 V and recharged, at the same current density, for half of the previous discharge time to reach 50% state-of-charge (SOC). Prior to polarization or further cycling, flow cell impedance was measured at open circuit potential over a frequency range of 200 kHz to 10 mHz with a potential amplitude of 10 mV and 5 measurements per frequency. To determine cell power performance, Galvanostatic polarization was performed with a 30 s hold per step, which allowed the cell to reach a steady state potential. Galvanostatic polarization was performed to determine cell power performance. Between each discharge step, the cell was recharged at 25 mA/cm^2 back to 50% SOC to maintain polarization accuracy. Immediately after polarization analysis, cell cycling experiments were performed at a constant current density of 100 mA/cm^2 for 40 cycles (experiment runtime of 2 d). For both polarization and cycling, potential limitations of 0.6 – 1.7 V were imposed.

Results and Analysis

Impact of PAN concentration and carbonization.—The main objective of this work was to produce fibrous electrodes with enhanced surface area by electrospinning mats with fibers much smaller than typical GDL materials, while avoid making fibers that were too small, which would result in low permeability. Computational modeling work had previously been undertaken to help determine a target fiber diameter[19] which suggested values around 1–2 μm. This is about 10× lower than conventional GDL materials but about 10× higher than typical electrospun materials.[16,22] One of the first challenges to address was how to electrospin fibers in this intermediate size range.

Polymer concentration plays a major role in the fiber diameter of electrospun mats,[35] with higher concentrations leading to thicker fibers. In order to produce the thickest possible fibers, the polymer concentration was increased to the highest values that could be spun without difficulty. Concentrations between 10 and 13 wt% were considered and basic analysis on both as-spun and carbonized mats were performed. SEM images of the electrospun mat before and after

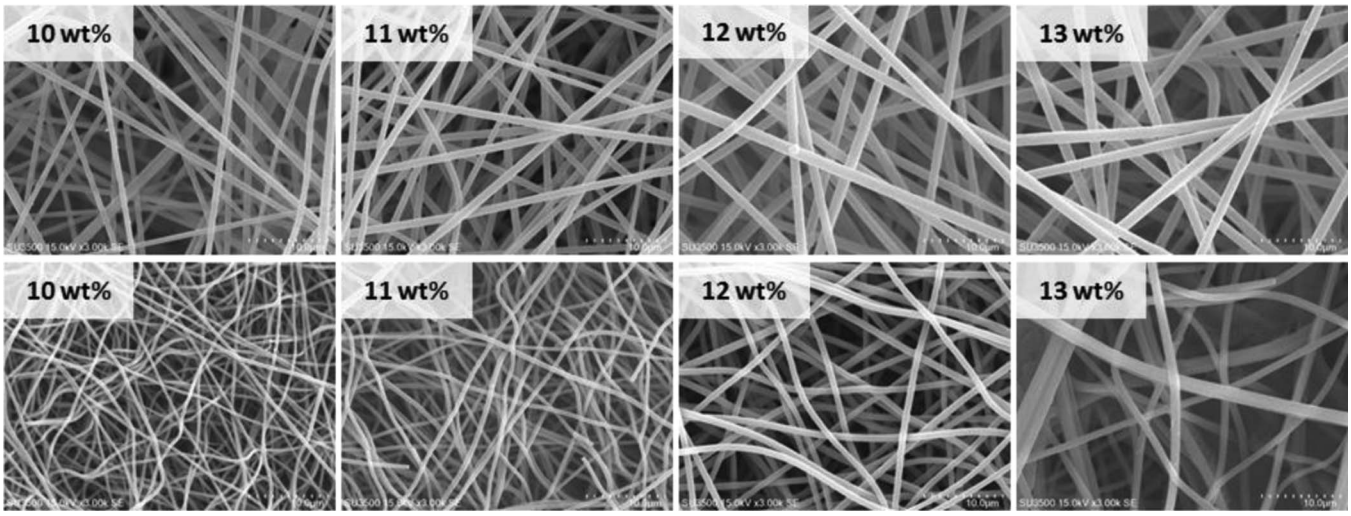

Figure 2. SEM images of electrospun samples on the top, and carbonized samples in the row below. All images are taken with magnification of 3000, and the scale bar is 10 μm.

carbonization for the varying polymer concentration can be seen in Figure 2.

Fiber diameter was measured for electrospun and carbonized mats and the results are shown in Figure 3 (left). As expected, fiber diameter, d_f, increases with higher polymer concentration. The d_f ranges from an average of 0.7 μm with 10 wt% to 1.4 μm with 13 wt%. During the carbonization step, the linear chains of PAN aromatize and form rings.[36] As material is lost in the carbonization process, the size of the electrospun mat decreases as shown in Figure 4. The weight of a mat typically decreases by about 50% after carbonization, and the thickness shrinks by about 20% to 30%. Because of this mass loss, the fiber diameter is expected to decrease after carbonization and this was observed in the SEM image analysis. For carbonized mats, d_f ranges from an average of 500 nm with 10 wt% to 1200 nm with 13 wt%. A calculation of fiber volumes (assumed as cylinders) per unit length based on these diameters suggests that indeed the values before and after correspond to approximately 50% reduction in solid volume. The skeletal density of the carbonized materials is ± 1.73 g/cm^3 on average, ranges from 1.55 to 2.14 g/ cm^3. This relatively wide range suggests that the degree of carbonization might have been inconsistent, and that higher furnace temperatures and/or longer treatment times might be worth further investigation in future work.

One of the ways to increase the permeability of a material with small fibers is to increase the porosity, as described by Eq. 5. Electrospinning is known to create very high porosity materials, with values typically above 90% which was part of its appeal for this investigation. The measured porosity of the present electrospun mats ranged from 96.6% to 92% from 10 wt% to 13% Figure 3 (right). The porosity decreases slightly with increasing polymer concentration, possibly because heavier fibers settle into a tighter mat during electrospinning. Upon carbonization, the porosity decreased by about 5% in absolute terms. This drop could be largely attributed to the fact that the mats are constrained between two alumina plates when placed into the furnace which means they are held in a compressed state during carbonization. The porosity of the carbonized mats was still quite high, well within the ranges suggested by the previous modeling[19] and much higher than typical GDL materials.[38]

Overall the 12 wt% was deemed as the most suitable for the production of electrospun electrodes, and this material is studied in more detail below and is referred to as EE-12. Polymer concentration higher than 12 wt% produced spinning solution that was too viscous, making the electrospinning process unstable and leading to the formation of large fiber bundles in the finished product. When carbonized the 12 wt% mats have an average fiber diameter of 765 nm with 89% porosity, which is close to the target values.[19]

Detailed characterization of target material.—In the previous section, it was demonstrated that the optimal PAN concentration was 12 wt%, as this created reasonably large fibers with high porosity, while still being manageable for production. In this section, this specific material is analyzed in greater detail to characterize all the relevant physical, structural, and transport properties. Additionally, the characterization tests were applied to the material before and after carbonization to evaluate the impact of the carbonization process on

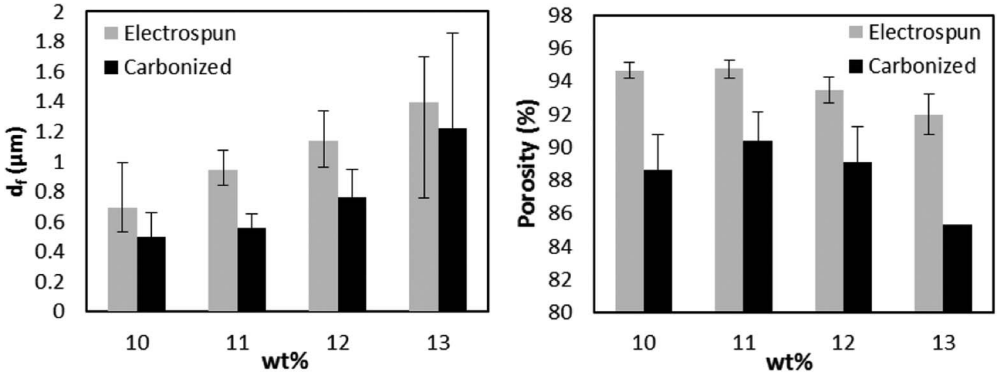

Figure 3. Effect of polymer concentration on fiber diameter (left) and porosity (right).

Figure 4. Images of electrospun PAN mat before and after carbonization.

the structure. The electrospun electrode made from 12 wt% PAN is referred to as EE-12 henceforth.

Specific surface area.—Surface area was measured using the BET method. Two samples of EE-12 were tested and the average surface area of the electrospun electrode was found to be 2.94 m^2/g. When adjusted by the bulk density of these materials, the average specific area is 505000 m^2/m^3. The theoretical specific surface area, derived from the filament analogue (FA) model using the porosity and fiber diameter were calculated and compared in Table II. The match between the BET measurement and the filament analogues is quite good, with only 10 to 20% error. This is a useful result as it means the filament analogue model is suitable as a first-order approximation of surface area, in numerical models of cell operation for instance.

The measured surface area for SGL 25AA and Toray 90, two typical electrode materials, were found to be 1.29 m^2/g and 0.217 m^2/g. The specific surface area for the EE-12 material was indeed higher than the typical electrode materials, meaning that the electrospinning approach successfully increased the surface area. Although the filament analogue model predicts the surface area of the Toray 090 material well, it fails to predict the surface area of SGL 25AA, giving a value 3 times lower than the measured value. When looking at SEM images of Toray 090 and SGL 25AA, a significant amount of particulate material can be seen coating the fibers of the SGL material. This particulate is known as binder, which is a polymer added to the precursor fiber structures prior to carbonization. The binder seems to increase the measured surface area substantially, which is not accounted for by the simple filament analogue model. Accurately gauging the surface area present inside the porous binder regions is quite difficult however. In terms of flow battery performance, it is of strong interest to know how much the internal surfaces in the binder region contribute to the electrochemical reaction, or whether these surfaces are starved of reactant since convective flow does not replenish them, but this is beyond the scope of the present work.

Electrical conductivity.—The electrical conductivity in the in-plane direction of the EE-12 material was found to be 1280 (±176) S/m. Using the same set up, the conductivity of SGL 25AA and Toray 90 was 3814 S/m and 16867 S/m, respectively. These two values agree with values reported in the literature, which proves the validity of the conductivity test.[46,47] The conductivity of EE-12 was lower than the commonly used GDLs, but still within the same order of magnitude and well above the conductivity of the electrolyte solutions, thus the resistance to electron transport will be an insignificant portion of the total ohmic polarization. Specifically, the conductivity of the redox active electrolyte used in this study (1.5 M $VOSO_4$ in 2.6 M H_2SO_4) is 44 S/m.

Table II. Summary of Specific Area Calculations.

	EE (1)	EE (2)	SGL 25AA	Toray 90	Freudenberg
porosity [%]	0.884	0.906	0.884	0.745	0.687
d_f [μm]	0.87	0.87	7.33	7.72	10
Bulk Density [g/cm^3]	0.196	0.154	0.202	0.478	0.54
BET A_s [m^2/g]	2.45	3.44	1.29	0.217	—
BET A_s [m^2/m^3]	480000	530000	261000	104000	—
FA A_s [m^2/m^3]	533000	432000	63300	132000	125000
% difference from FA	−10.1	22.6	313.2	−21.4	—

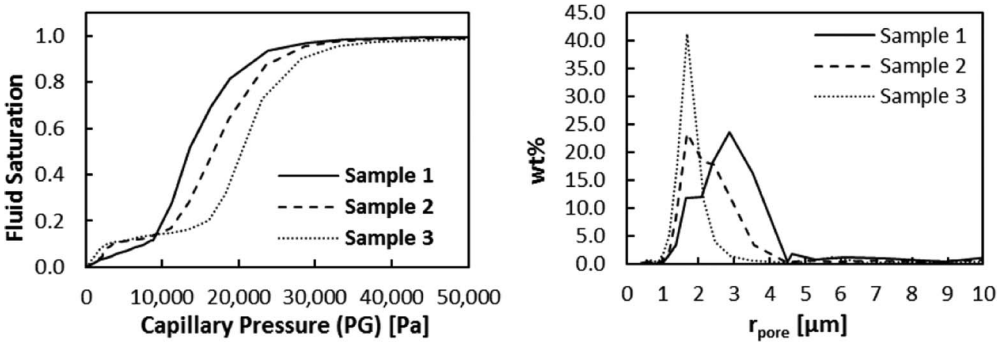

Figure 5. Capillary pressure curves (left) and pore size distribution histograms (right) obtained by draining a wetting fluid from the pore space by injection of air.

The lower conductivity of the EE-12 material is also expected based on the higher porosity, and hence lower solid volume fraction present to carry electric charge. Increasing the final carbonization temperature is known to increase the conductivity of carbonized PAN,[48] so this could be explored if higher values are sought. The relatively good electrical conductivity suggests that the carbonization protocol was sufficient to produce fully carbonized materials.

Pore size distributions.—Porosimetry was applied to the EE-12 materials, yielding the results shown in Figure 5. Capillary curves and pore size distribution were obtained for multiple samples from the same sheet of electrospun mat, but carbonized in different batches. These samples showed some variation. Additional samples with varying polymer concentration and therefore fiber diameter were also tested, but the results were similar to those already shown, so they are not included. Pore sizes did not vary depending on fiber diameter, and the average pore radius varied from 1.5 to 3 microns for all samples. For comparison the pore sizes in SGL 25AA and Toray 090 are typically greater than 30 microns.[49]

Permeability coefficient.—In-plane permeability as a function of compression was measured before and after carbonization. As expected, permeability decreased with increasing compression, since porosity and open space for flow is reduced. This trend was observed for both electrospun and carbonized materials as seen in Figure 6. Samples were taken at 2 perpendicular directions on the mat to determine the extent of anisotropy in the material. The material produced was slightly anisotropic, which may be attributed the direction of the rotating drum. For the purpose of this analysis, we have assumed that the material is isotropic, and the slight variation in the measurement is due to the variation in samples.

At first glance, the permeability, K, behaves very similarly before and after carbonization. For example, at about 80% compressed porosity, both electrospun and carbonized mat have a permeability constant of around $K = 2 \times 10^{-13}$ m^2. Despite the changes to porosity and fiber diameter that have occurred during carbonization, the permeability of the material did not change significantly. This is surprising since the Carmen-Kozeny relationship given in Eq. 5 shows that the permeability should change with fiber diameter, porosity and k_{ck}. This suggests the morphology of the fibers and their structure changed during carbonization, which would be accounted for a by a change in the Carman-Kozeny constant, k_{ck}.

Given the measured porosity and fiber diameter of the electrospun and carbonized mats, values of k_{ck} were calculated for each permeability datum. As seen in Figure 6 the k_{ck} was not constant with compression, which was seen previously[18] for electrospun mats. The change in k_{ck} was attributed to non-uniform distribution of strain within the sample during compression, resulting in a high porosity (high permeability) region in the center of the sample and a lower porosity (low permeability) region near the surfaces where the sample holder was contacting the sample. This behavior of changing k_{ck} was observed to be true also for the carbonized EE-12. Another reason that could explain this decrease in k_{ck} with compression is a change in the structure or morphology due to fiber deformation or breakage. As seen in Figure 7, SEM images are taken of the electrode material before and after compression in the permeability holder. For an uncarbonized material, fibers appeared to be deformed after compression. This means that more fibers are in contact with each other, closing off pores, and some have changed from cylinders to a flattened ribbon. For the carbonized EE-12 material many fibers appear broken, which might cause permeability to increase due to more pathways for flow through the structure.

A representative value of k_{ck} can be obtained by extrapolating back to the uncompressed porosity of the material.[18] Following this procedure, the average projected k_{ck} of the electrospun mat was around 10, and that of carbonized mats was around 6. This decrease in k_{ck} indicates the change in structure during the carbonization step. A lower k_{ck} indicates a more permeable structure, which explains how the fiber diameter and porosity decreased in the EE-12 with little effect on the overall permeability. The k_{ck} values measured here are higher than the previously reported value of 2,[18] as well as the values of 4.5 reported by Tomadakis and Robertson.[15] The higher k_{ck} found in this work may be due to the increase in fiber diameter from around 300 nm to around 1100 nm causing some effect that is not captured in the Carman-Kozeny model. Another possible reason is erroneous fiber diameter measurement, which was obtained by analyzing SEM images of fibers on the surface, which may differ from the internal fibers.

Vanadium flow battery performance.—All-vanadium flow cell performance is shown in Figure 8 using pristine samples of EE-12 and Sigracet SGL 25AA. We opted to use pristine carbon samples here to examine the performance without any additional treatment. Investigation an optimal treatment strategy for the EE materials is ongoing, so in the present study untreated samples were used to ensure a more fare and direct comparison.

Figure 8a shows the Nyquist plot, generated from electrochemical impedance spectroscopy of full cells at 50% SOC and open circuit voltage (OCV), containing either EE-12 or SGL 25AA electrodes. The observed spectra shows two arcs, in agreement with prior reports,[50] which have been attributed to charge-transfer resistance of the redox reactions on the electrode surfaces (higher frequency arc) and mass transfer resistance in the porous electrodes (lower frequency arc). While both cells provide similar characteristic responses, the overall resistance (low frequency) of the cell containing EE-12 is three-fold less than the cell containing SGL 25AA. While the electrical resistivity of the SGL 25AA is significantly lower than the EE-12 (12.9 S/cm, Table I vs. 3.5 – 4 S/cm for 29AA, which is replacement product for SGL 25AA with similar properties but less manufacturing variability), the ohmic resistances, represented by the high frequency intercepts on the Nyquist plots, are nearly identical. This indicates that solid phase electrode resistivity is only a minor contributor to cell ohmic resistance. In contrast to the SGL 25AA spectra, the low frequency intercept in the spectra of the EE-12 closely matches the

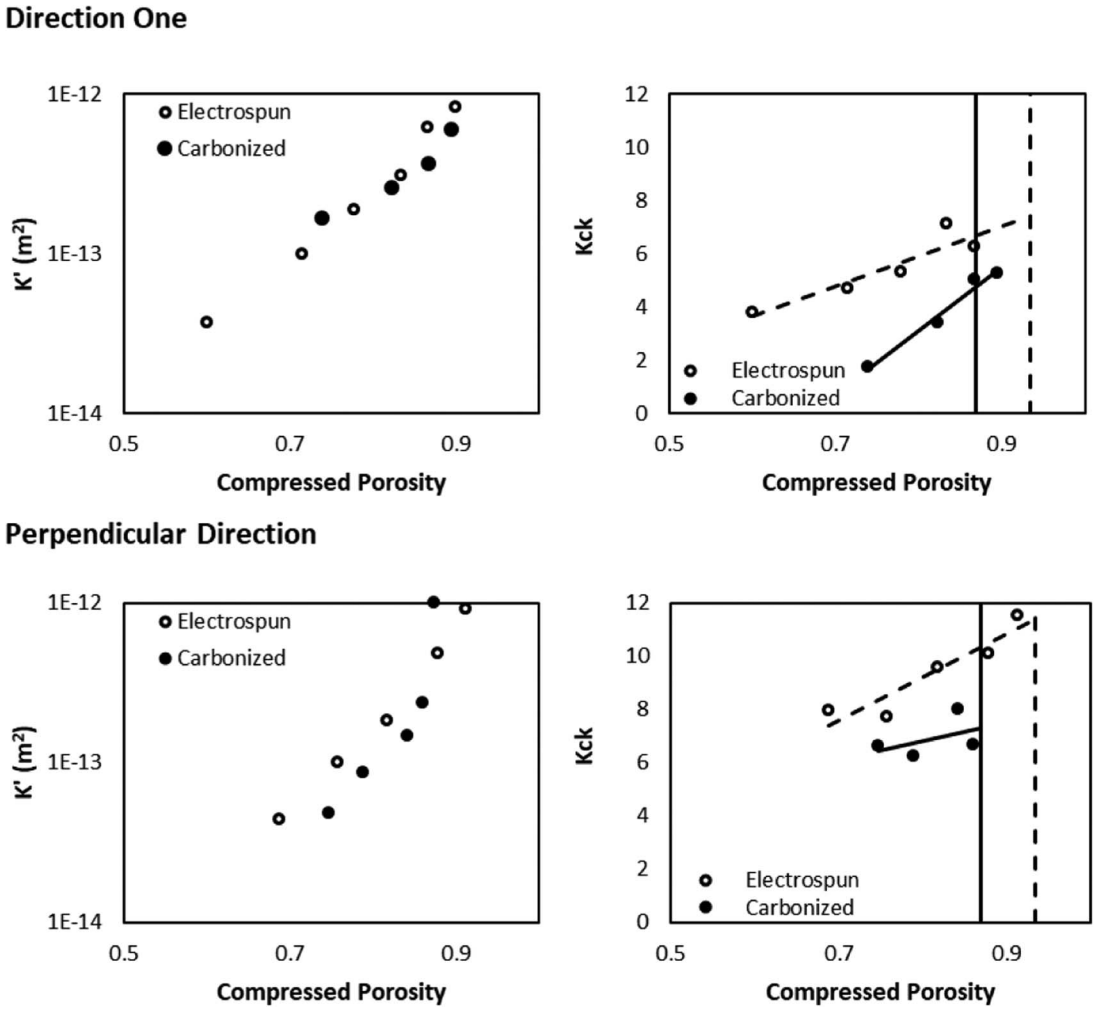

Figure 6. In-plane permeability comparison for electrospun and carbonized mats. The top row and the bottom row are experiments done on samples with orthogonal direction from the same sheet of material. The effect of compression on permeability is the on the left, and the effect of compression on k_{CK} is on the right. The vertical lines in the right graphs are the uncompressed porosities.

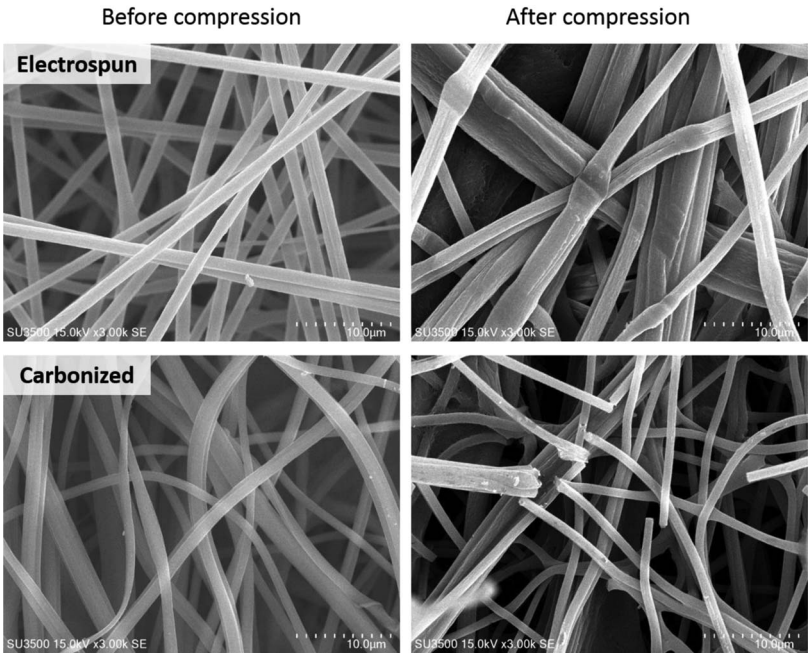

Figure 7. Effect of compression on fiber morphology for electrospun (top two images) and carbonized samples. All images are of sample made with the same 13 wt% concentration spinning solution.

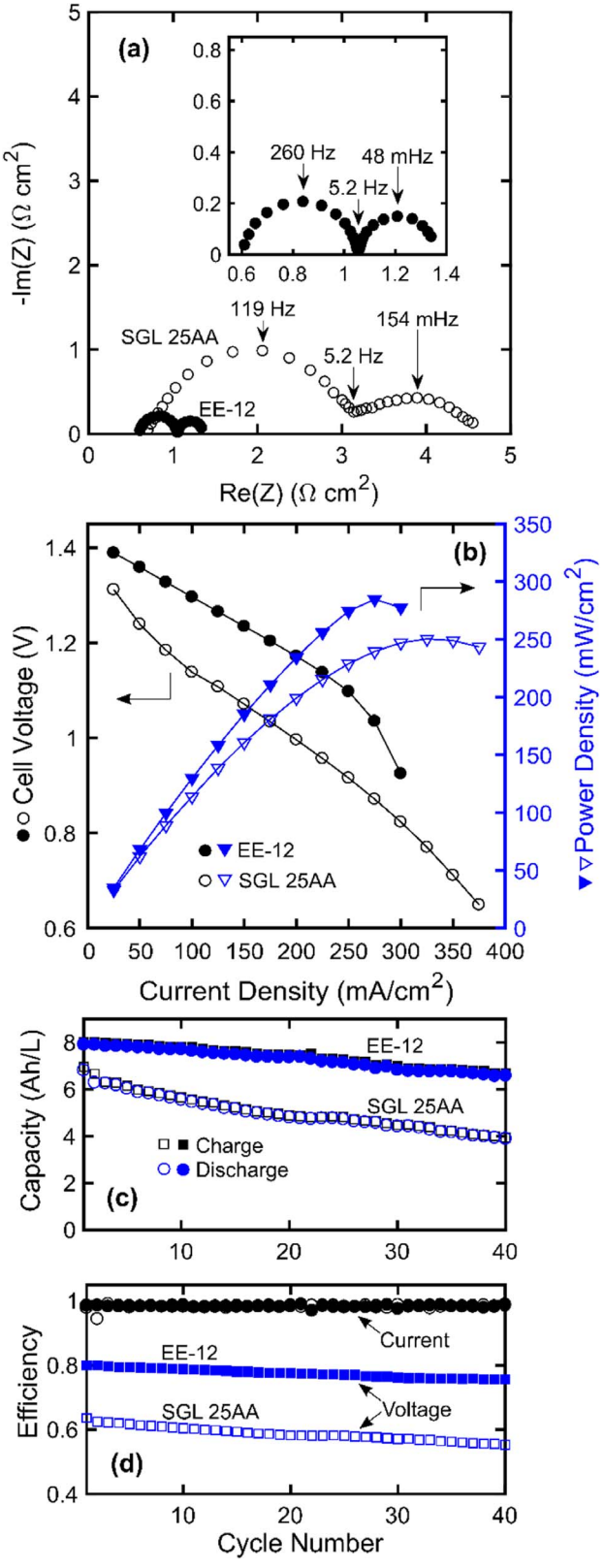

Figure 8. All-vanadium flow battery performance. Filled symbols are used for EE-12 and open symbols are used for SGL 25AA throughout. a) Nyquist impedance at 50% SOC for EE-12 and SGL 25AA. Inset plot shows details of EE-12. b) Polarization and power curves at 50% SOC. c) Volumetric capacity as a function of cycle number. Theoretical capacity is 20.1 Ah/L. d) Current and voltage efficiency as a function of cycle number. Energy efficiency was omitted as it nearly overlays the voltage efficiency due to the high current efficiency.

cell ASR calculated by applying Ohm's law to the polarization data below 100 mA/cm^2 (Figure 8b). This difference illustrates the poor vanadium charge transfer resistance, which has coupled contributions from active area and surface-specific kinetics, as pristine SGL 25AA requires a greater potential bias to drive the faradaic reactions. In contrast, the vanadium redox charge transfer resistance on EE-12 is sufficiently small as to be described at open circuit conditions. Poor vanadium redox kinetics on carbon electrodes are well-known in the literature[51–53] and have motivated research into pretreatments (e.g., thermal oxidation, acid soak) that can improve the kinetic response through increased surface area or modifying surface chemistry. The reduced charge-transfer resistance of the EE-12, illustrated by the impedance spectra and polarization curve, suggests that the additional surface area in the EE-12 material was beneficial and indicates that such pretreatments may not be necessary for this electrode. This does not preclude the possibility that pretreatments could improve the performance even further. We also note that mass transfer resistance is reduced with the use of EE-12 as compared to SGL 25AA which we attribute to smaller pore sizes that reduce the diffusion length scale.

Figure 8b shows polarization and power density curves, at 50% SOC, where, in agreement with the open circuit impedance data, the cell with EE-12 outperforms the cell with SGL 25AA electrodes largely due to reduced charge transfer resistance. The peak power density for EE-12, 285 mW/cm^2 at 275 mA/cm^2, and for SGL 25AA, 250 mW/cm^2 at 325 mA/cm^2, both of which are below state-of-the-art values but within the range of previously reported values.[6,9,54] Surprisingly, at high current densities, greater mass transfer limitations are observed with the EE-12 as compared to the SGL 25AA; in contrast to our expectations for this high-surface area electrode as well as the common interpretation of the low-frequency arc on the Nyquist plot (Figure 8a). There are several possible causes for this result. It could arise from heterogeneity of the EE-12 material structure leading to higher flow rates in some locations and by-passing elsewhere. Such by-passing, or channeling, of the flow would also occur if the material were not uniformly compressed, since the permeability is a strong function of compressed porosity as shown in Figure 6. At low current densities (Figure 8b), only partial electrode utilization occurs whether the entire electrode is accessible via advection. However, at high current densities, where a large fraction of the electrode is utilized, this phenomenon becomes apparent and thus mass transfer limitations are observed.

The cell capacity and efficiency are plotted for 40 cycles at a current density of 100 mA/cm^2 in Figure 8c and Figure 8d, respectively. The EE-12 accessed substantially more capacity than SGL 25AA; initially 8 Ah/L vs 6 Ah/L, and this spread increased with cycling to 6.5 Ah/L vs 4 Ah/L. While both cells exhibited similar current efficiencies > 98%, the EE-12 has a higher voltage efficiency due to the reduced kinetic and mass transfer resistances. This observation suggests that even with partial utilization, the EE-12 can outperform pristine SGL 25AA and access a larger fraction of the theoretical capacity (20.1 Ah/L based on 1.5 M vanadium in two 10 mL reservoirs) than SGL 25AA. Electrode engineering to improve the homogeneity of the electrospun materials can further enhance this performance, particularly at high current densities and extreme states of charge. Furthermore, surface activation treatments were not investigated here, so significant further performance gains could be had for the EE materials.

Conclusions

A custom-made fibrous electrospun electrode (EE) was produced with the aim of increasing reactive surface area and thereby improving cell efficiency and performance. Previous modeling work had suggested that fibers sizes around 1 micron and porosities above 0.85 could provide a several-fold boost in cell performance, so these materials properties were targeted. Electrospinning was used to make the materials since this technique required minimal sophisticated equipment or tooling. One challenge was to produce fibers that were large enough, since most electrospinning research aims to produced fibers as small as possible. Polyacrylonitrile was electrospun in various

weight-percent solutions in an attempt to make fibers with a diameter on the order of 1–2 micron, and a concentration of 12 wt% had a low enough viscosity to be easily and stably produced, while high concentrations were difficult to work with. The materials were carbonized using literature procedures with no significant challenges. The structural and transport properties (fiber diameter, porosity pore size, surface area, permeability and electrical conductivity) of the materials before and after carbonization were extensively studied, using a suite of experimental tools developed for fuel cell gas diffusion layers due to their similarity. The 12 wt% material had the desired properties, with 3× more surface area than SGL 25AA, yet maintained a reasonable permeability due to its much higher porosity. The absolute permeability of the PAN materials and the carbonized EE-12 materials surprisingly showed similar values despite a significant change in fiber size and porosity after carbonization. This suggests that the structure of the material was somehow altered during carbonization, possible by burning and removal of very small fibers. The electrical conductivity was lower than SGL 25AA, because it had higher porosity (less solid volume for conduction), but typically in electrochemical systems the electrical conductivity is not important since most ohmic loss occurs in the electrolyte phase.

Cell-level performance tests showed that the EE-12 electrode showed substantially lower activation resistance, which could be at least partly due to the increased surface area. No surface treatments were applied to either the EE-12 or the SGL 25AA samples. Surface activation is known to improve the apparent kinetics of the SGL 25AA material, so presumably some form of treatment could be could be applied to the EE-12 material as well. However, surface treatment to carbonized electrospun electrodes was beyond the scope of the present work. Despite better all-round performance, the EE-12 showed limiting current behavior earlier than the SGL 25AA. This was attributed to heterogeneity in the pore structure creating regions of low permeability that were by-passed by the flow. Under low current conditions these regions would be replenished with reactant at a sufficient rate by diffusion, but at higher currents they would become starved of reactant and give rise to concentration polarization.

Overall the EE-12 electrode performed very well and represents an improvement over off-the-shelf SGL 25AA materials. Many optimizations and improvements could still be made, but this first attempt showed promise. Future work should focus on developing surface treatments that improve the kinetics or enhance the liquid-solid contact. It also remains unclear why the EE-12 material showed worse performance at high currents, but the favored hypothesis is that structural heterogeneity could be a problem. Future production of EE materials should focus on ensuring a more stable and repeatable production process, consistent fiber size, and uniform thickness.

Acknowledgments

The funding for this research was provided by the NSERC Discovery grant and Post-Graduate Scholarship programs, and by the Eugenie-Ulmer Lamothe Fund of Department of Chemical Engineering at McGill. Flow cell testing in this work was funded by the Joint Center for Energy Storage Research (JCESR) managed by Argonne National Laboratory.

References

1. A. Z. Weber, M. M. Mench, J. P. Meyers, P. N. Ross, J. T. Gostick, and Q. Liu, "Redox flow batteries: a review," *J. Appl. Electrochem.*, **41**(10), 1137 (2011).
2. P. Alotto, M. Guarnieri, and F. Moro, "Redox flow batteries for the storage of renewable energy: A review," *Renew. Sustain. Energy Rev.*, **29**, 325 (2014).
3. L. H. Thaller, "Electrically rechargeable REDOX flow cell," US3996064 A, 07-Dec-1976.
4. R. M. Darling, K. G. Gallagher, J. A. Kowalski, S. Ha, and F. R. Brushett, "Pathways to low-cost electrochemical energy storage: a comparison of aqueous and nonaqueous flow batteries," *Energy Environ. Sci.*, **7**(11), 3459 (2014).
5. R. Dmello, J. D. Milshtein, F. R. Brushett, and K. C. Smith, "Cost-driven materials selection criteria for redox flow battery electrolytes," *J. Power Sources*, **330**, 261 (2016).
6. D. S. Aaron et al., "Dramatic performance gains in vanadium redox flow batteries through modified cell architecture," *J. Power Sources*, **206**, 450 (2012).
7. K. T. Cho, P. Ridgway, A. Z. Weber, S. Haussener, V. Battaglia, and V. Srinivasan, "High Performance Hydrogen/Bromine Redox Flow Battery for Grid-Scale Energy Storage," *J. Electrochem. Soc.*, **159**(11), A1806 (2012).
8. M. C. Tucker, K. T. Cho, A. Z. Weber, G. Lin, and T. V. Nguyen, "Optimization of electrode characteristics for the Br2/H2 redox flow cell," *J. Appl. Electrochem.*, **45**(1), 11 (2014).
9. I. Mayrhuber, C. R. Dennison, V. Kalra, and E. C. Kumbur, "Laser-perforated carbon paper electrodes for improved mass-transport in high power density vanadium redox flow batteries," *J. Power Sources*, **260**, 251 (2014).
10. G. Lin et al., "Advanced Hydrogen-Bromine Flow Batteries with Improved Efficiency, Durability and Cost," *J. Electrochem. Soc.*, **163**(1), A5049 (2016).
11. V. Yarlagadda, G. Lin, P. Y. Chong, and T. V. Nguyen, "High Surface Area Carbon Electrodes for Bromine Reactions in H2-Br2 Fuel Cells," *J. Electrochem. Soc.*, **163**(1), A5126 (2016).
12. A. M. Pezeshki, J. T. Clement, G. M. Veith, T. A. Zawodzinski, and M. M. Mench, "High performance electrodes in vanadium redox flow batteries through oxygen-enriched thermal activation," *J. Power Sources*, **294**, 333 (2015).
13. R. Carta, S. Palmas, A. M. Polcaro, and G. Tola, "Behaviour of a carbon felt flow by electrodes Part I: Mass transfer characteristics," *J. Appl. Electrochem.*, **21**(9), 793 (1991).
14. G. W. Jackson and D. F. James, "The permeability of fibrous porous media," *Can. J. Chem. Eng.*, **64**(3), 364 (1986).
15. M. M. Tomadakis and T. J. Robertson, "Viscous Permeability of Random Fiber Structures: Comparison of Electrical and Diffusional Estimates with Experimental and Analytical Results," *J. Compos. Mater.*, **39**(2), 163 (2005).
16. J. T. Gostick, M. W. Fowler, M. D. Pritzker, M. A. Ioannidis, and L. M. Behra, "In-plane and through-plane gas permeability of carbon fiber electrode backing layers," *J. Power Sources*, **162**(1), 228 (2006).
17. P. H. Nelson, "Permeability-porosity Relationships In Sedimentary Rocks," *Log Anal.*, **35**(03), (1994).
18. M. D. R. Kok and J. T. Gostick, "Transport properties of electrospun fibrous membranes with controlled anisotropy," *J. Membr. Sci.*, **473**, 237 (2015).
19. M. D. R. Kok, A. Khalifa, and J. T. Gostick, "Multiphysics Simulation of the Flow Battery Cathode: Cell Architecture and Electrode Optimization," *J. Electrochem. Soc.*, **163**(7), A1408 (2016).
20. Z.-M. Huang, Y.-Z. Zhang, M. Kotaki, and S. Ramakrishna, "A review on polymer nanofibers by electrospinning and their applications in nanocomposites," *Compos. Sci. Technol.*, **63**(15), 2223 (2003).
21. E. Frank, L. M. Steudle, D. Ingildeev, J. M. Spörl, and M. R. Buchmeiser, "Carbon Fibers: Precursor Systems, Processing, Structure, and Properties," *Angew. Chem. Int. Ed.*, **53**(21), 5262 (2014).
22. T. Wang and S. Kumar, "Electrospinning of polyacrylonitrile nanofibers," *J. Appl. Polym. Sci.*, **102**(2), 1023 (2006).
23. L. Zhang, A. Aboagye, A. Kelkar, C. Lai, and H. Fong, "A review: carbon nanofibers from electrospun polyacrylonitrile and their applications," *J. Mater. Sci.*, **49**(2), 463 (2013).
24. E. Fitzer, W. Frohs, and M. Heine, "Optimization of stabilization and carbonization treatment of PAN fibres and structural characterization of the resulting carbon fibres," *Carbon*, **24**(4), 387 (1986).
25. E. Zussman et al., "Mechanical and structural characterization of electrospun PAN-derived carbon nanofibers," *Carbon*, **43**(10), 2175 (2005).
26. S. Y. Gu, J. Ren, and Q. L. Wu, "Preparation and structures of electrospun PAN nanofibers as a precursor of carbon nanofibers," *Synth. Met.*, **155**(1), 157 (2005).
27. Y. Yang, F. Simeon, T. A. Hatton, and G. C. Rutledge, "Polyacrylonitrile-based electrospun carbon paper for electrode applications," *J. Appl. Polym. Sci.*, **124**(5), 3861 (2012).
28. X. Mao, T. A. Hatton, and G. C. Rutledge, "A Review of Electrospun Carbon Fibers as Electrode Materials for Energy Storage," *Curr. Org. Chem.*, **17**(13), 1390 (2013).
29. B. Zhang, F. Kang, J.-M. Tarascon, and J.-K. Kim, "Recent advances in electrospun carbon nanofibers and their application in electrochemical energy storage," *Prog. Mater. Sci.*, **76**, 319 (2016).
30. S. Peng et al., "Electrospun carbon nanofibers and their hybrid composites as advanced materials for energy conversion and storage," *Nano Energy*, **22**, 361 (2016).
31. S. Cavaliere, S. Subianto, I. Savych, D. J. Jones, and J. Rozière, "Electrospinning: designed architectures for energy conversion and storage devices," *Energy Environ. Sci.*, **4**(12), 4761 (2011).
32. G. Wei, J. Liu, H. Zhao, and C. Yan, "Electrospun carbon nanofibres as electrode materials toward VO2+/VO2+ redox couple for vanadium flow battery," *J. Power Sources*, **241**, 709 (2013).
33. A. Fetyan et al., "Electrospun Carbon Nanofibers as Alternative Electrode Materials for Vanadium Redox Flow Batteries," *ChemElectroChem*, **2**(12), 2055 (2015).
34. U. Ali, X. Wang, and T. Lin, "Effect of nozzle polarity and connection on electrospinning of polyacrylonitrile nanofibers," *J. Text. Inst.*, **103**(11), 1160 (2012).
35. S. Y. Gu, J. Ren, and G. J. Vancso, "Process optimization and empirical modeling for electrospun polyacrylonitrile (PAN) nanofiber precursor of carbon nanofibers," *Eur. Polym. J.*, **41**(11), 2559 (2005).
36. M. S. A. Rahaman, A. F. Ismail, and A. Mustafa, "A review of heat-treatment on polyacrylonitrile fiber," *Polym. Degrad. Stab.*, **92**(8), 1421 (2007).
37. P. Trogadas et al., "X-ray micro-tomography as a diagnostic tool for the electrode degradation in vanadium redox flow batteries," *Electrochem. Commun.*, **48**, 155 (2014).
38. R. R. Rashapov, J. Unno, and J. T. Gostick, "Characterization of PEMFC Gas Diffusion Layer Porosity," *J. Electrochem. Soc.*, **162**(6), F603 (2015).

39. J. T. Gostick, M. A. Ioannidis, M. W. Fowler, and M. D. Pritzker, "Direct measurement of the capillary pressure characteristics of water–air–gas diffusion layer systems for PEM fuel cells," *Electrochem. Commun.*, **10**(10), 1520 (2008).
40. J. T. Gostick, M. A. Ioannidis, M. W. Fowler, and M. D. Pritzker, "Wettability and capillary behavior of fibrous gas diffusion media for polymer electrolyte membrane fuel cells," *J. Power Sources*, **194**(1), 433 (2009).
41. H. Giesche , "Mercury Porosimetry: A General (Practical) Overview," *Part. Part. Syst. Charact.*, **23**, 9 (2006).
42. L. J. Van der Pauw, "A Method of measuring the resistiviy and Hall Coefficient on Lamellae of Arbitrary Shape," *Philips Tech. Rev.*, **26**, 220 (1958).
43. J. D. Milshtein, J. L. Barton, R. M. Darling, and F. R. Brushett, "4-acetamido-2,2,6,6-tetramethylpiperidine-1-oxyl as a model organic redox active compound for nonaqueous flow batteries," *J. Power Sources*, **327**, 151 (2016).
44. J. D. Milshtein et al., "High current density, long duration cycling of soluble organic active species for non-aqueous redox flow batteries," *Energy Environ. Sci.*, **9**(11), 3531 (2016).
45. J. D. Milshtein, S. L. Fisher, T. M. Breault, L. T. Thompson, and F. R. Brushett, "Feasibility of a Supporting-Salt-Free Nonaqueous Redox Flow Battery Utilizing Ionic Active Materials," *ChemSusChem*, p. n/a-n/a, Jan. 2017.
46. I. Nitta, T. Hottinen, O. Himanen, and M. Mikkola, "Inhomogeneous compression of PEMFC gas diffusion layer: Part I. Experimental," *J. Power Sources*, **171**(1), 26 (2007).
47. D. Natarajan and T. Van Nguyen, "Effect of electrode configuration and electronic conductivity on current density distribution measurements in PEM fuel cells," *J. Power Sources*, **135**(1–2), 95 (2004).
48. Z. Zhou et al., "Development of carbon nanofibers from aligned electrospun polyacrylonitrile nanofiber bundles and characterization of their microstructural, electrical, and mechanical properties," *Polymer*, **50**(13), 2999 (2009).
49. I. V. Zenyuk, D. Y. Parkinson, L. G. Connolly, and A. Z. Weber, "Gas-diffusion-layer structural properties under compression via X-ray tomography," *J. Power Sources*, **328**, 364 (2016).
50. C.-N. Sun, F. M. Delnick, D. S. Aaron, A. B. Papandrew, M. M. Mench, and T. A. Zawodzinski, "Resolving Losses at the Negative Electrode in All-Vanadium Redox Flow Batteries Using Electrochemical Impedance Spectroscopy," *J. Electrochem. Soc.*, **161**(6), A981 (2014).
51. B. Sun and M. Skyllas-Kazacos, "Modification of graphite electrode materials for vanadium redox flow battery application—I. Thermal treatment," *Electrochimica Acta*, **37**(7), 1253 (1992).
52. B. Sun and M. Skyllas-Kazacos, "Chemical modification of graphite electrode materials for vanadium redox flow battery application—part II. Acid treatments," *Electrochimica Acta*, **37**(13), 2459 (1992).
53. M.-A. Goulet, M. Skyllas-Kazacos, and E. Kjeang, "The importance of wetting in carbon paper electrodes for vanadium redox reactions," *Carbon*, **101**, 390 (2016).
54. C. Zhang, T. S. Zhao, Q. Xu, L. An, and G. Zhao, "Effects of operating temperature on the performance of vanadium redox flow batteries," *Appl. Energy*, **155**, 349 (2015).